Semester project

Optimal flapping and pitching motion of NACA airfoils for thrust generation

by Barde Paul

Ecole polytechnique fédérale de Lausanne
Section Génie Mécanique
Laboratoire de mécanique des fluides et instabilités
François Gallaire, Simon Pasche and Francesco Viola
January 8, 2016

Contents

List of Figures

Introduction

The following project is based on two former semester projects, [1, 2], where the thrust generated by a flapping [1] and pitching [2] airfoil has been studied. In this work, the combined flapping/pitching motion is investigated. This is a more realistic representation of biological propulsion and may find applications in many fields such as robotics, bio mechanical systems design, etc..
In particular, the main point is to understand the effect on thrust generation of the phase-shift between the flapping and the pitching motion.

The results are based on numerical simulations carried out with the software `nek5000` which implements the spectral elements method (SEM). The numerical tools are similar to the ones developed by [1] and [2] and we refer to these works for details on the mesh generation and implementation in `nek5000`.
Specifically, we have considered a flipping/pitching NACA0012 subjected to an incoming flow at Reynolds $Re = 100$. For the two motion the frequency of oscillation is fixed to $St = 1$, while the flapping and pitching amplitudes are respectively $A = 0.3$ and $\theta_0 = 0.16$. The phase shift between the pitching and the flapping motion is the remaining parameter which is varied in order to determine the optimal phase angle corresponding to the maximum thrust and lift generation. Moreover the lift generation associated to symmetry breaking is investigated and discussed.

1 Navier-Stokes equations in a non inertial frame

1.1 Reference frames

The airfoil is subjected to two motions: a harmonic displacement along the vertical direction, $\boldsymbol{j}$ and a harmonic rotation around a point located at one tenth of the chord length. Therefore, the center of rotation is also moving along the $\boldsymbol{j}$ direction. We consider two reference frames: the inertial one $(O, \boldsymbol{ijk})$ and the non-inertial frame $(\widehat{O}, \widehat{\boldsymbol{ijk}})$ attached to the airfoil, see Fig. 1.1. The $\boldsymbol{k}$ and $\widehat{\boldsymbol{k}}$ directions coincide and are pointed toward the reader.

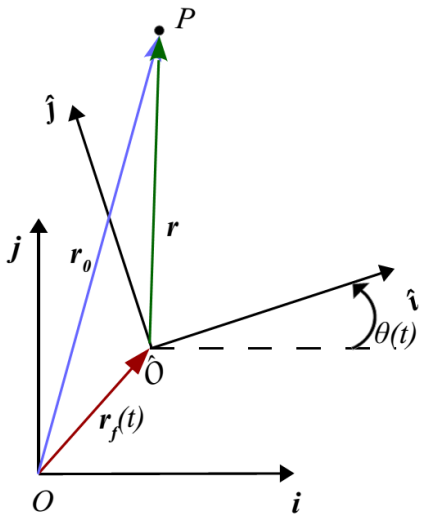

Figure 1.1: Inertial and non inertial frames

The following geometrical relations hold between the two frames:

$$\begin{cases} \widehat{\boldsymbol{i}} = \cos(\theta)\,\boldsymbol{i} + \sin(\theta)\,\boldsymbol{j} \\ \widehat{\boldsymbol{j}} = -\sin(\theta)\,\boldsymbol{i} + \cos(\theta)\,\boldsymbol{j} \\ \widehat{\boldsymbol{k}} = \boldsymbol{k} \end{cases} \quad \text{and} \quad \begin{cases} \boldsymbol{i} = \cos(\theta)\,\widehat{\boldsymbol{i}} - \sin(\theta)\,\widehat{\boldsymbol{j}} \\ \boldsymbol{j} = \sin(\theta)\,\widehat{\boldsymbol{i}} + \cos(\theta)\,\widehat{\boldsymbol{j}} \\ \boldsymbol{k} = \widehat{\boldsymbol{k}} \end{cases} \tag{1.1}$$

Specifically, the position of a point P, that is fixed in the inertial frame, appears to be moving in the non inertial one :

$$\begin{aligned} \boldsymbol{r} &= \widehat{x}\widehat{\boldsymbol{i}} + \widehat{y}\widehat{\boldsymbol{j}} \\ &= [(x - x_f)\cos(\theta) + (y - y_f)\sin(\theta)]\,\widehat{\boldsymbol{i}} + [-(x - x_f)\sin(\theta) + (y - y_f)\cos(\theta)]\,\widehat{\boldsymbol{j}} \end{aligned} \tag{1.2}$$

Due to the combined harmonic motion which is imposed to the airfoil, the non-inertial frame translates and rotates with respect to the inertial one according to:

$$\mathbf{r}_f(t) = \frac{A_0}{2}\cos(\omega t + \alpha)\,\boldsymbol{j} \qquad \boldsymbol{\theta}(t) = \theta_0 \cos(\phi t)\,\boldsymbol{k} \tag{1.3}$$

1.2 Governing equations

1.2.1 Velocity and acceleration in a non-inertial frame

The velocity of a particle can be decomposed in the following way:

$$\mathbf{v} = \mathbf{v}_f + \mathbf{v}_{rel} + \boldsymbol{\Omega} \times \mathbf{r} \tag{1.4}$$

where $\mathbf{v}$ is the total velocity of the particle, $\mathbf{v}_f$ is the translation velocity of the moving frame with respect to the inertial one, $\mathbf{v}_{rel}$ is the velocity of the particle relative to the moving frame, $\boldsymbol{\Omega}$ is the rotation of the moving frame and $\mathbf{r}$ is the position of the considered particle in the moving frame. Given the motion of the foil (1.3) and the relation between the two frames (1.1):

$$\mathbf{v}_f = v_f \boldsymbol{j} = v_f(\sin(\theta)\,\widehat{\boldsymbol{i}} + \cos(\theta)\,\widehat{\boldsymbol{j}}) \qquad \boldsymbol{\Omega} \times \mathbf{r} = \Omega\widehat{\boldsymbol{k}} \times (\widehat{x}\widehat{\boldsymbol{i}} + \widehat{y}\widehat{\boldsymbol{j}}) = \Omega\widehat{x}\widehat{\boldsymbol{i}} - \Omega\widehat{y}\widehat{\boldsymbol{j}} \tag{1.5}$$

and,

$$\mathbf{v} = (v_f \sin(\theta) + \widehat{u}_{\widehat{x}} - \Omega\widehat{y})\widehat{\boldsymbol{i}} + (v_f \cos(\theta) + \widehat{u}_{\widehat{y}} + \Omega\widehat{x})\widehat{\boldsymbol{j}} \tag{1.6}$$

with $(\widehat{u}_x, \widehat{u}_y)$, $(\widehat{x}, \widehat{y})$, the velocities, respectively the coordinates, in the non inertial frame.

Similarly, the acceleration of a particle (i.e the material derivative of the velocity) is decomposed:

$$\frac{D\mathbf{v}}{Dt} = \mathbf{a}_f + \mathbf{a}_{rel} + 2\boldsymbol{\Omega} \times \mathbf{v}_{rel} + \dot{\boldsymbol{\Omega}} \times \mathbf{r} + \boldsymbol{\Omega} \times (\boldsymbol{\Omega} \times \mathbf{r}) \tag{1.7}$$

with $\mathbf{a}_f$ the translation acceleration of the moving frame with respect to the inertial one, $\mathbf{a}_{rel} = \dfrac{D\mathbf{v}_{rel}}{Dt}$ the acceleration of the particle with respect to the non inertial frame. The three additional terms are, form left to right, the Coriolis acceleration, the Euler acceleration and the centrifugal acceleration.

From the definition of the flapping displacement given in (1.3) it yields:

$$\mathbf{v}_f = \dot{\mathbf{r}}_f = -\frac{A_0}{2}\omega \sin(\omega t + \alpha)\,\boldsymbol{j} \qquad \text{and} \qquad \mathbf{a}_f = \dot{\mathbf{v}}_f = -\frac{A_0}{2}\omega^2 \cos(\omega t + \alpha)\,\boldsymbol{j} \tag{1.8}$$

And from the definition of pitching in (1.3):

$$\boldsymbol{\Omega} = \dot{\theta} = -\phi\theta_0 \sin(\phi t)\,\widehat{\boldsymbol{k}} \qquad \text{and} \qquad \dot{\boldsymbol{\Omega}} = -\phi^2\theta_0 \cos(\phi t)\,\widehat{\boldsymbol{k}} \tag{1.9}$$

Hence:

$$\begin{aligned}
-\mathbf{a}_f &= \frac{A_0}{2}\omega^2 \cos(\omega t+\alpha)\, \sin(\theta)\, \widehat{\boldsymbol{i}} + \frac{A_0}{2}\omega^2 \cos(\omega t+\alpha)\, \cos(\theta)\, \widehat{\boldsymbol{j}} \\
-2\boldsymbol{\Omega}\times\mathbf{v}_{rel} &= -2\Omega\widehat{\boldsymbol{k}}\times(\widehat{u}_{\widehat{x}}\widehat{\boldsymbol{i}}+\widehat{u}_{\widehat{y}}\widehat{\boldsymbol{j}}) = 2\Omega(\widehat{u}_{\widehat{y}}\widehat{\boldsymbol{i}}-\widehat{u}_{\widehat{x}}\widehat{\boldsymbol{j}}) \\
-\dot{\boldsymbol{\Omega}}\times\mathbf{r} &= -\dot{\Omega}\widehat{\boldsymbol{k}}\times(\widehat{x}\widehat{\boldsymbol{i}}+\widehat{y}\widehat{\boldsymbol{j}}) = \dot{\Omega}(\widehat{y}\widehat{\boldsymbol{i}}-\widehat{x}\widehat{\boldsymbol{j}}) \\
-\boldsymbol{\Omega}\times(\boldsymbol{\Omega}\times\mathbf{r}) &= -\Omega\widehat{\boldsymbol{k}}\times(\Omega\widehat{\boldsymbol{k}}\times(\widehat{x}\widehat{\boldsymbol{i}}+\widehat{y}\widehat{\boldsymbol{j}}) = \Omega^2(\widehat{x}\widehat{\boldsymbol{i}}+\widehat{y}\widehat{\boldsymbol{j}})
\end{aligned} \tag{1.10}$$

1.2.2 Navier-Stokes in a non-inertial frame

Let's consider the Navier-Stokes equation in an inertial frame for an newtonian and incompressible fluid:

$$\frac{D\mathbf{v}}{Dt} = -\frac{1}{\rho}\boldsymbol{\nabla}p + \nu\nabla^2\mathbf{v} \tag{1.11}$$

Using (1.4) and (1.7):

$$\frac{D\mathbf{v}_{rel}}{Dt} + \mathbf{a}_f + 2\boldsymbol{\Omega}\times\mathbf{v}_{rel} + \dot{\boldsymbol{\Omega}}\times\mathbf{r} + \boldsymbol{\Omega}\times(\boldsymbol{\Omega}\times\mathbf{r}) = -\frac{1}{\rho}\boldsymbol{\nabla}p + \nu\nabla^2(\mathbf{v}_f + \mathbf{v}_{rel} + \boldsymbol{\Omega}\times\mathbf{r}) \tag{1.12}$$

The Laplacian operator is linear and the term $\nabla^2\mathbf{v}_f$ vanishes because the frame's translation is independent of the position. Moreover, $\boldsymbol{\Omega}\times\mathbf{r}$ is linear in the spatial coordinates, hence $\nabla^2(\boldsymbol{\Omega}\times\mathbf{r})$ is null. In addition, the pressure does not depend on the reference frame. Thus, (1.12) reads:

$$\frac{D\mathbf{v}_{rel}}{Dt} + \mathbf{a}_f + 2\boldsymbol{\Omega}\times\mathbf{v}_{rel} + \dot{\boldsymbol{\Omega}}\times\mathbf{r} + \boldsymbol{\Omega}\times(\boldsymbol{\Omega}\times\mathbf{r}) = -\frac{1}{\rho}\boldsymbol{\nabla}p + \nu\nabla^2\mathbf{v}_{rel} \tag{1.13}$$

We recall that the spatial differentiation of scalars $p(x,t)$ and vectors $\mathbf{v}(x,t)$ is invariant: $\nabla p = \nabla' p$ and $\nabla\mathbf{v} = \nabla'\mathbf{v}$, where ∇' is the gradient in the non-inertial frame. Hence, equation (1.13) in the non-inertial frame reads:

$$\begin{cases}
\dfrac{D\mathbf{v}_{rel}}{Dt} = -\dfrac{1}{p}\boldsymbol{\nabla}p + \nu\nabla^2\mathbf{v}_{rel} + ff_{\widehat{x}}\widehat{\boldsymbol{i}} + ff_{\widehat{y}}\widehat{\boldsymbol{j}} \\
\quad ff_{\widehat{x}} = \dfrac{A_0}{2}\omega^2 \cos(\omega t+\alpha)\, \sin(\theta_0\cos(\phi t)) - 2\phi\theta_0 \sin(\phi t)\, \widehat{u}_{\widehat{y}} ... \\
\qquad ... - \phi^2\theta_0 \cos(\phi t)\, \widehat{y} + (\phi\theta_0 \sin(\phi t))^2\widehat{x} \\
\quad ff_{\widehat{y}} = \dfrac{A_0}{2}\omega^2 \cos(\omega t+\alpha)\, \cos(\theta_0\cos(\phi t)) + 2\phi\theta_0 \sin(\phi t)\, \widehat{u}_{\widehat{x}} ... \\
\qquad ... + \phi^2\theta_0 \cos(\phi t)\, \widehat{x} + (\phi\theta_0 \sin(\phi t))^2\widehat{y}
\end{cases} \tag{1.14}$$

Similarly, the continuity equation for an incompressible fluid reads:

$$\boldsymbol{\nabla}\cdot\mathbf{v} = \boldsymbol{\nabla}\cdot(\mathbf{v}_f + \mathbf{v}_{rel} + \boldsymbol{\Omega}\times\mathbf{r}) = 0 \tag{1.15}$$

Here again, since the motion does not depend on the position the $\boldsymbol{\nabla}\cdot\mathbf{v}_f$ term falls. Direct calculation also results in $\boldsymbol{\nabla}\cdot(\boldsymbol{\Omega}\times\mathbf{r}) = 0$.

Finally the continuity equation holds in the non-inertial frame:

$$\boldsymbol{\nabla}\cdot\mathbf{v} = \boldsymbol{\nabla}\cdot\mathbf{v}_{rel} = 0 \tag{1.16}$$

1.3 Boundary conditions

The boundary condition specifying the velocity at the inlet (subscript bc) in the moving frame reads:

$$\mathbf{v}|_{bc} = U\boldsymbol{i} = U(\cos(\theta)\,\widehat{\boldsymbol{i}} - \sin(\theta)\,\widehat{\boldsymbol{j}}) \tag{1.17}$$

So, using (1.6) to express the corresponding velocity in the non-inertial frame, it follows:

$$\begin{aligned}\mathbf{v}_{rel}|_{bc} = &\left[U\cos(\theta_0\cos(\phi t)) + \frac{A_0}{2}\omega\sin(\omega t+\alpha)\,\sin(\theta_0\cos(\phi t)) - \phi\theta_0\sin(\phi t)\,\widehat{y}\right]\widehat{\boldsymbol{i}}... \\ &... + \left[-U\sin(\theta_0\cos(\phi t)) + \frac{A_0}{2}\omega\sin(\omega t+\alpha)\,\cos(\theta_0\cos(\phi t)) + \phi\theta_0\sin(\phi t)\,\widehat{x}\right]\widehat{\boldsymbol{j}}\end{aligned} \tag{1.18}$$

1.4 Initial condition

In the numerical simulation (DNS) we assume that the initial velocity around the foil is given by Eq. (1.18) evaluated at $t = 0$. This is equivalent to assume that the foil just "appears" in the fluid with a horizontal velocity of U and starts its oscillating motion. In order to investigate the flow dynamics at regime, the simulation time has to be larger than the initial transient state which depends on the initial condition. However, in the case of "symmetry breaking regimes" the initial condition will effect the solution also at regime, see section 4.

1.5 Aerodynamic forces

The drag, D, and lift, L, in the inertial frame are related to the drag, D_{rel} and the lift, L_{rel} of the moving frame according to:

$$\begin{cases} D = D_{rel}\cos(\theta) - L_{rel}\sin(\theta) = D_{rel}\cos(\theta_0\cos(\phi t)) - L_{rel}\sin(\theta_0\cos(\phi t)) \\ L = D_{rel}\sin(\theta) + L_{rel}\cos(\theta) = D_{rel}\sin(\theta_0\cos(\phi t)) + L_{rel}\cos(\theta_0\cos(\phi t)) \end{cases} \tag{1.19}$$

1.6 Vorticity

The vorticity depends on the reference frame. The vorticity in the absolute frame, $\nabla\times\mathbf{v}$, is related to the one in the non-inertial frame according to:

$$\nabla\times\mathbf{v} = \nabla\times\mathbf{v}_f + \nabla\times\mathbf{v}_{rel} + \nabla\times(\boldsymbol{\Omega}\times\mathbf{r}) \tag{1.20}$$

The first term on the right hand side is null because the translation of the moving frame is independent of the location. Eventually,

$$\nabla\times\mathbf{v} = \nabla\times\mathbf{v}_{rel} - 2\phi\theta_0\sin(\phi t)\,\widehat{\boldsymbol{k}} \tag{1.21}$$

1.7 Normalization

The characteristic quantities of the system are:

$$Re = \frac{Uc}{\nu} \quad St_\omega = \frac{\omega c}{2\pi U} \quad St_\phi = \frac{\phi c}{2\pi U} \quad A = \frac{A_0}{c} \tag{1.22}$$

where, U and c are respectively the velocity of the incoming flow and the chord length of the foil. Here, they are arbitrarily set to one:

$$U = c = 1 \tag{1.23}$$

which yields:

$$Re = \frac{1}{\nu} \quad St_\omega = \frac{\omega}{2\pi} \quad St_\phi = \frac{\phi}{2\pi} \quad A = A_0 \tag{1.24}$$

Finally, as a reminder we show the configuration of the problem in figure 1.2.

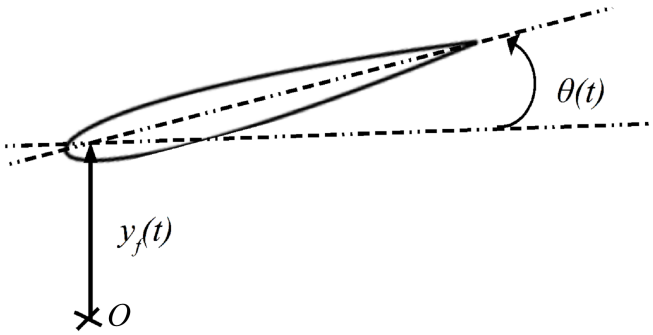

Figure 1.2: Foil configuration

2 Validation of the numerical tools

2.1 Nek5000 & Gambit

In this work the governing equations are discretized and integrated in time using the software `Nek5000` [3] which implements the spectral elements method. The mesh is generated using the **ANSYS** software `Gambit` [4]. First, the domain is partitioned using a `matlab` script. This enables the user to preferentially refine chosen regions such as the boundary layer. The parameters enabling this tuning are defined in the appendix, see Fig. A.1. The output mesh of `Gambit` is then converted into `Nek`'s mesh format. A particular attention is granted during this process in order to accurately convert the curved elements. Indeed, `Gambit` uses polynomial functions to approximate the curved elements whereas `Nek` uses circle's arcs. For further informations regarding the meshing routine the reader is referred to the following works: [1] and [2].

2.2 Boundary conditions assessment

In this section we will investigate the dependence on the boundary conditions. The following parameters are considered here:

- $\theta_0 = 0.12$
- $\alpha = \pi$
- $N = 60$
- $A = 0.4$
- $Re = 100$
- $l_b = 12$
- $St_\omega = St_\phi = St = 0.3$
- $\mathbf{lx1} = 9$
- $h_b = 14$

The chosen phase-shift yields to an initial vertical position of the foil at $-A$. **lx1** is the degree of the polynomial (in both $\widehat{x}$ and $\widehat{y}$ directions) used by `Nek5000`. N is the number of elements as defined by the `matlab` script `meshing.m`. l_b and h_b are respectively the length and height of the domain. This set of parameters induces a Karman vortex street that is almost aligned, see Fig. 2.5. The comparison between the different boundary conditions is carried out on the lift and drag coefficients. We see that the solution is transient and that we must wait a certain time, around four time units, for the solution to be at regime. A typical solution is shown in Fig. 2.1.

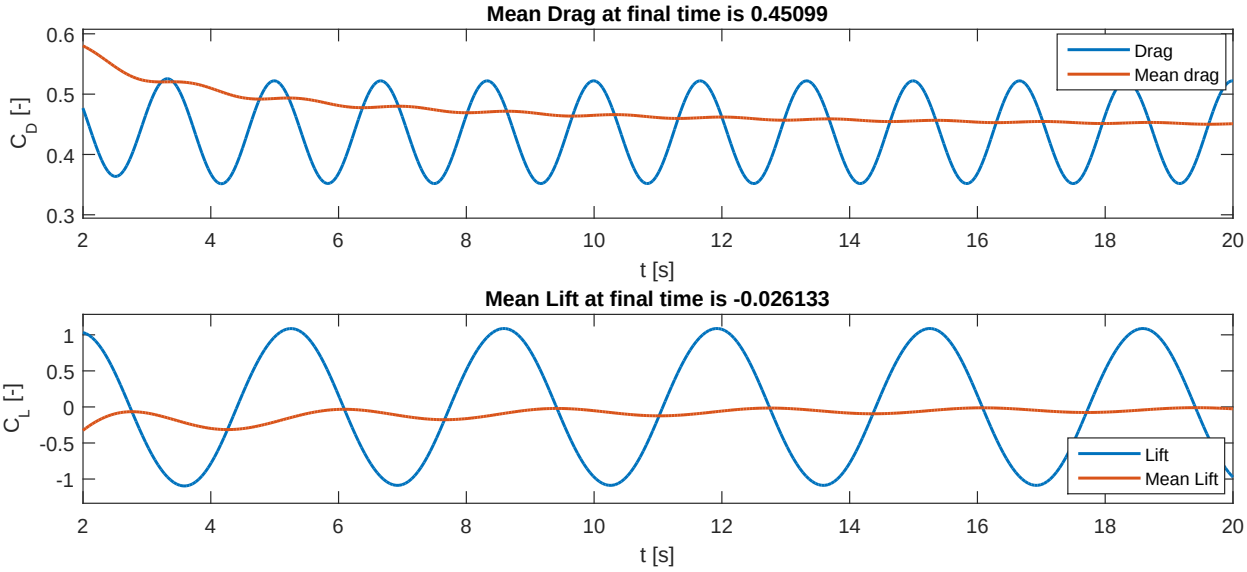

Figure 2.1: At regime aerodynamic and mean aerodynamic forces for vOOO BC

We see that the forces are periodic, therefore it is interesting to define the temporal averaged value for a force $F(t)$:

$$\bar{F}(t) = \frac{1}{t - t_i} \int_{t_i}^{t} F(s)\, ds \tag{2.1}$$

As we can see on figure 2.1 (where we set $t_i = 0$), the transient part (not plotted here) influences the mean value. The mean lift, for example, is in this case non-zero. Therefore we shall set $t_i = 4$ s in order to capture only the part at regime. Moreover, we take an integer number of periods to accurately compute the mean values. $t_{fd} = t_s + \frac{4}{St}$ for the drag and $t_{fl} = t_s + \frac{4}{2St}$ for the lift. We find then:

$$\bar{C}_D(t_{fd}) = 0.43704 \qquad \bar{C}_L(t_{fl}) = -2.8369 \times 10^{-4} \tag{2.2}$$

The null lift was expected since the situation displays a top down symmetry. We can also find the frequency of oscillation (see figure A.2 in appendix):

$$St_D = 0.6001 \approx 2St \qquad St_L = 0.3 \approx St \tag{2.3}$$

The frequencies of the aerodynamic forces are linked to the vortex shedding frequency: one vortex is shed from the top of the foil when it moves up and one vortex is shed from the bottom of the foil when is goes down. This constitutes the vortex shedding process of period St. On the one hand, the drag acting on the foil is the same (from symmetry) for a vortex shed from the top or the bottom of the foil, therefore the periodicity occurs every time a vortex is shed, i.e. two times per cycle: the frequency is multiplied by two. On the other hand, the lift orientation depends on which side the vortex is shed and the lift has therefore the same frequency than the vortex shedding.

2.2.1 vOOO boundary condition

As a starting point we try the boundary conditions illustrated in figure 2.2.

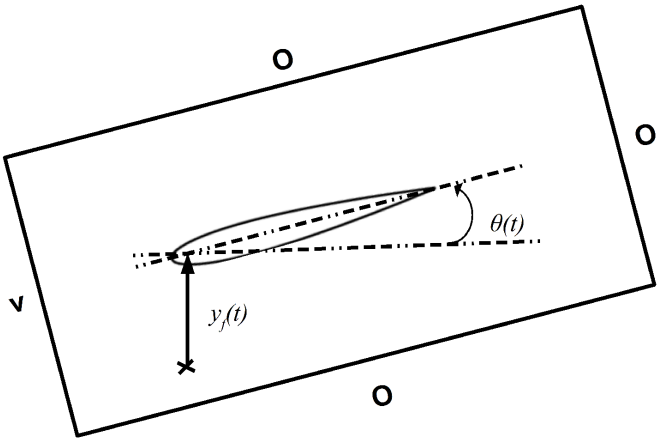

Figure 2.2: vOOO boundary configuration

We use the notation of `Nek5000` where v indicates a Dirichlet boundary condition: we impose the inlet velocity. In our case the velocity is given by equation (1.18). The O boundary conditions, stand for free stress. By doing this we do not impose any constraint on the flow and this is the less restrictive configuration.

2.2.2 vvvO boundary condition

This boundary conditions are similar to the vOOO ones but here we impose the velocity on the upper and lower part of the domain, see Fig. 2.3. This is a bit more restrictive than previously.

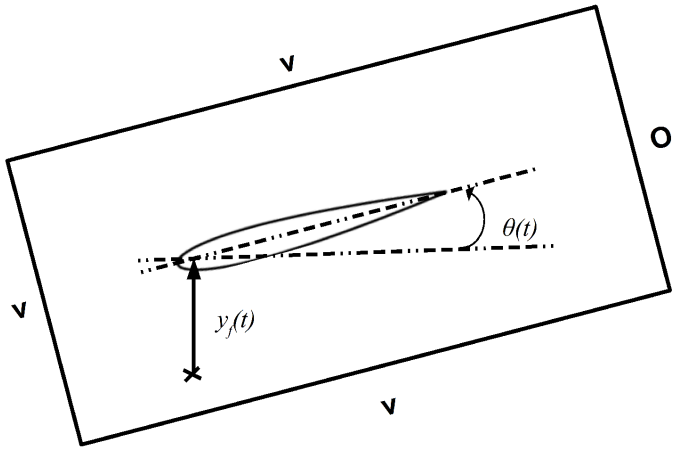

Figure 2.3: vvvO boundary configuration

2.2.3 vvvv boundary condition

These boundary conditions are really restrictive and we can observe that they generate disturbances in the flow behind the foil, see Fig. 2.5. As a matter of fact the vortices shed by the foil arrive at the boundary behind the foil and do not meet the imposed inlet velocity.

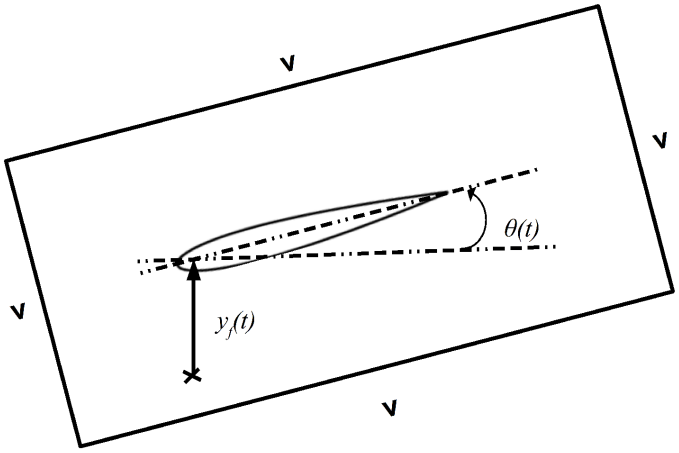

Figure 2.4: vvvv boundary configuration

2.2.4 Comparison

In the considered case the three set of boundary conditions work well and agree: see Tab. 2.1, Fig. 2.5 and Fig. 2.6. However, due to numerical instabilities, vvvO and vOOO do not converge for higher amplitudes and frequencies of the harmonic motions. This might be due to the O boundary condition which is defined in `Nek5000` as [3, p. 32] :

$$[-p\mathbf{I} + \nu\nabla\mathbf{u}]\,\mathbf{n} = 0 \tag{2.4}$$

This latter should be modified to take into account the non inertial reference frame. More specifically, the vector normal to the boundary, $\mathbf{n}$, should be modified to take into account the harmonic motion of the boundary.

Because of these convergence issues we will use the vvvv boundary condition from now on. But vvvv require to impose the velocity on all the boundaries and results in instabilities in the far field, see Fig. 2.5. This calls for a converge analysis: in the next section we investigate the effect of the mesh refinement and of the polynomials' degree. Then, in section 4, the effect of the domain size is discussed.

BC	$\mathbf{St_D}$	$\mathbf{St_L}$	$\mathbf{\bar{C}_D}$	$\mathbf{\bar{C}_L} \times 10^4$
vOOO	0.6001	0.3	0.43704	-2.8369
vvvO	0.6001	0.3	0.4371	-4.2151
vvvv	0.6002	0.3	0.43713	-11.475

Table 2.1: Comparison for the forces and frequencies

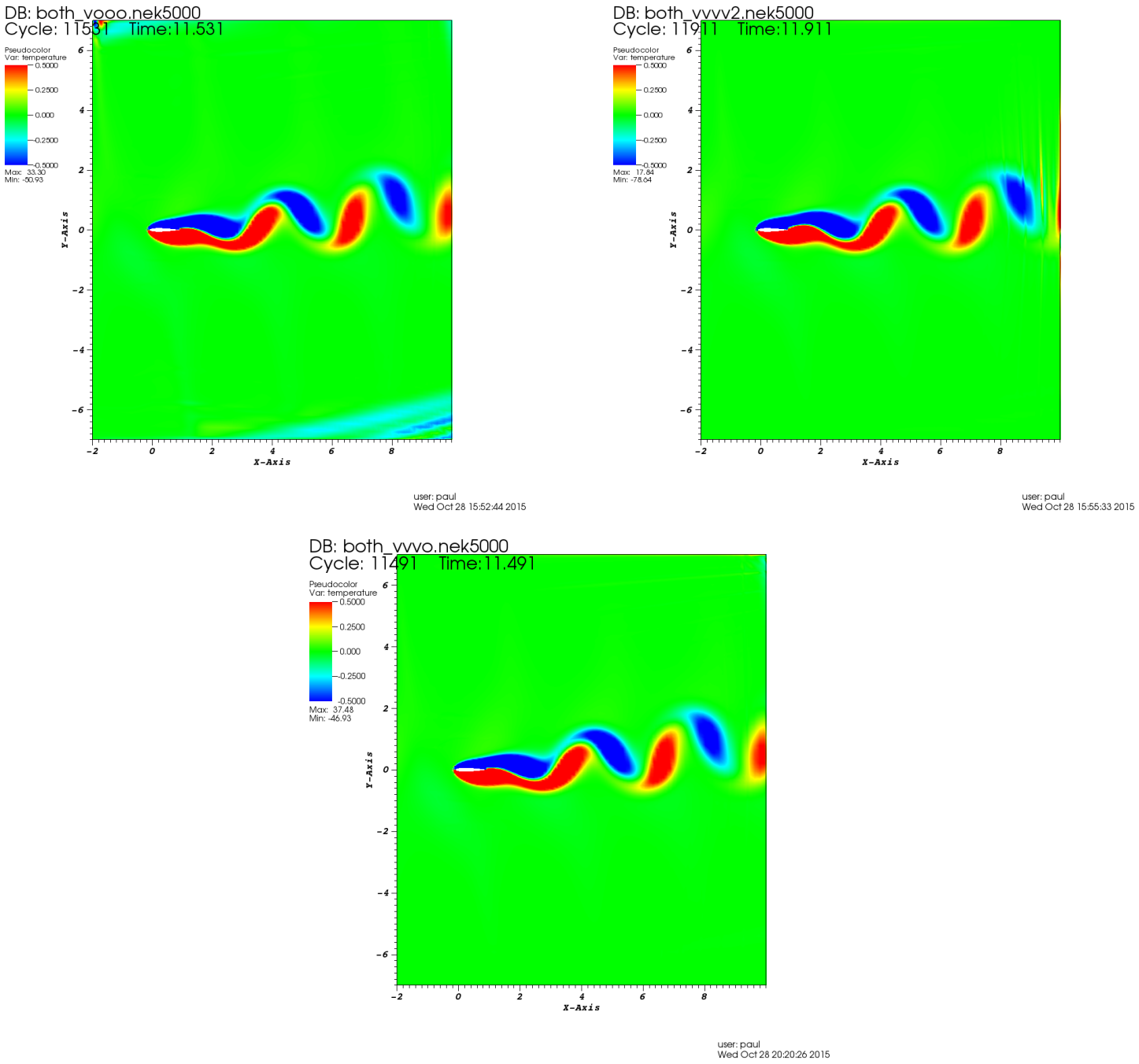

Figure 2.5: Flow patterns (absolute vorticity)

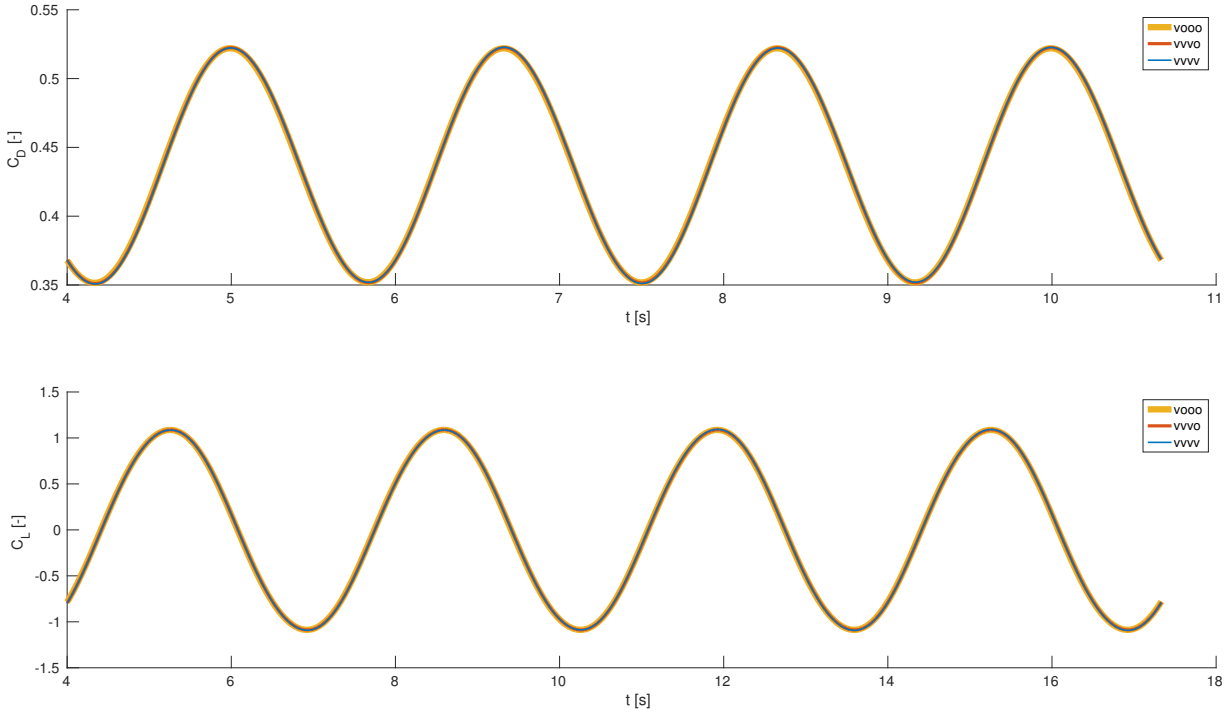

Figure 2.6: Comparison of at regime solutions between the boundary conditions

It is interesting to notice that, at regime, the solution for the aerodynamic forces seem to be a sinus or a cosinus. At first sight this might be obvious since we disturb the system with sinusoidal motions. Yet, since we are solving the non-linear Navier-Stokes equations the forcing terms are not directly linked to the solution, therefore we can not claim the solution to be a sinusoidal function. However this would be the case if we were in the low Reynold regime were the Navier-Stokes equations become the linear Stokes equations.

3 Convergence analysis

The convergence analysis is carried out with the following parameters:

- $\theta_0 = 0.16$
- $St_\omega = St_\phi = St = 1$
- $Re = 100$
- $A = 0.3$
- $\alpha = \frac{\pi}{2}$

We will vary both the number of elements in the mesh and the degree of the polynomials. The different parameters allowing for the tuning of the mesh cells' distribution is displayed in figure A.1. For the curved domains, the horizontal number of elements refers to the number of elements in the layers parallel to the surface and the vertical number of elements refers to the number of elements in the layers normal to the surface.

For this convergence analysis we will pay a particular attention to the values $\bar{C}_D(t_f)$, $\bar{C}_L(t_f)$, St_D and St_L. The time required for the simulation, t, will also be looked at. **ld**, the degree of the polynomials for the convective terms is kept equal to $\frac{3}{2}$**lx1**. We have to define quantities such

as the relative elapsed time and the global error. The most accurate solution is obviously the one with highest mesh elements and polynomials' degree. Let's label its values as follow:

$$\bar{C}_D^*(t_f) \qquad \bar{C}_L^*(t_f) \qquad St_D^* \qquad St_L^* \qquad t^* \tag{3.1}$$

Then, the total error is defined as:

$$e = \sqrt{\left((\frac{\bar{C}_D^*(t_f) - \bar{C}_D(t_f)}{\bar{C}_D^*(t_f)}\right)^2 + \left(\frac{\bar{C}_L^*(t_f) - \bar{C}_L(t_f)}{\bar{C}_L^*(t_f)}\right)^2 + \left(\frac{St_D^* - St_D}{St_D^*}\right)^2 + \left(\frac{St_L^* - St_L}{St_L^*}\right)^2} \tag{3.2}$$

And the relative elapsed time:

$$\epsilon_t = \frac{t - t^*}{t^*} \tag{3.3}$$

We will also consider the error done on the different values independently, from (3.2):

$$e = \sqrt{e_D^2 + e_L^2 + e_{StD}^2 + e_{StL}^2} \tag{3.4}$$

3.1 vvvv boundary condition

With the considered set of parameters we have an interesting flow pattern with a reversed von Karman vortex street, see fig. 3.1. We will see that this configuration generates thrust.

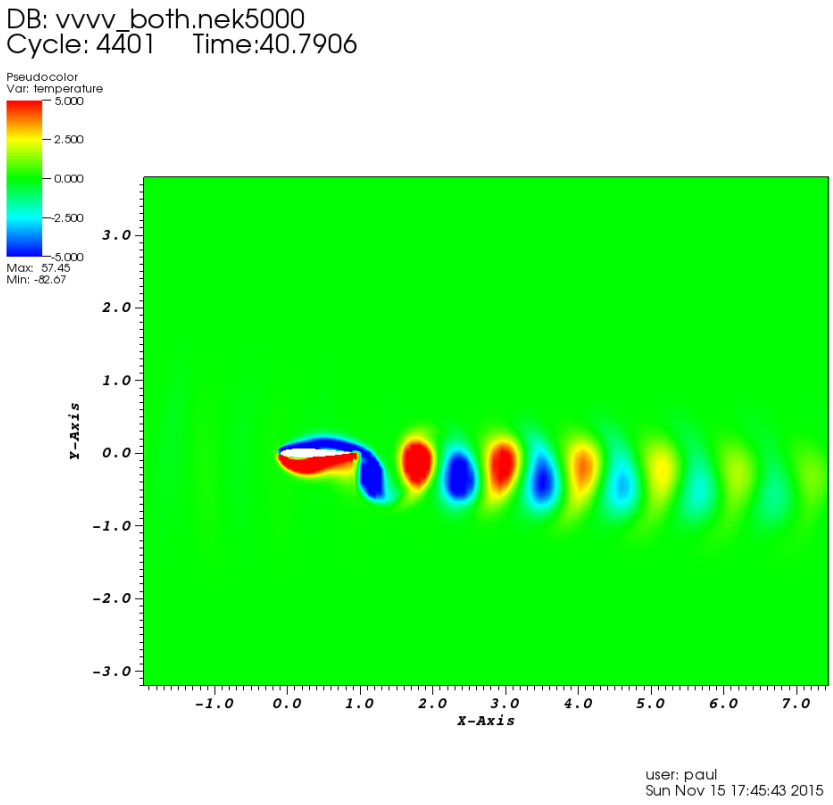

Figure 3.1: Reversed von Karman vortex street (absolute vorticity)

As we can see from fig. 3.2 the solutions at regime converge toward the most accurate one. The two solutions ($N = 60$, **lx1** $= 9$) and ($N = 120$, **lx1** $= 6$) are rather close with a slight advantage for the finer mesh.

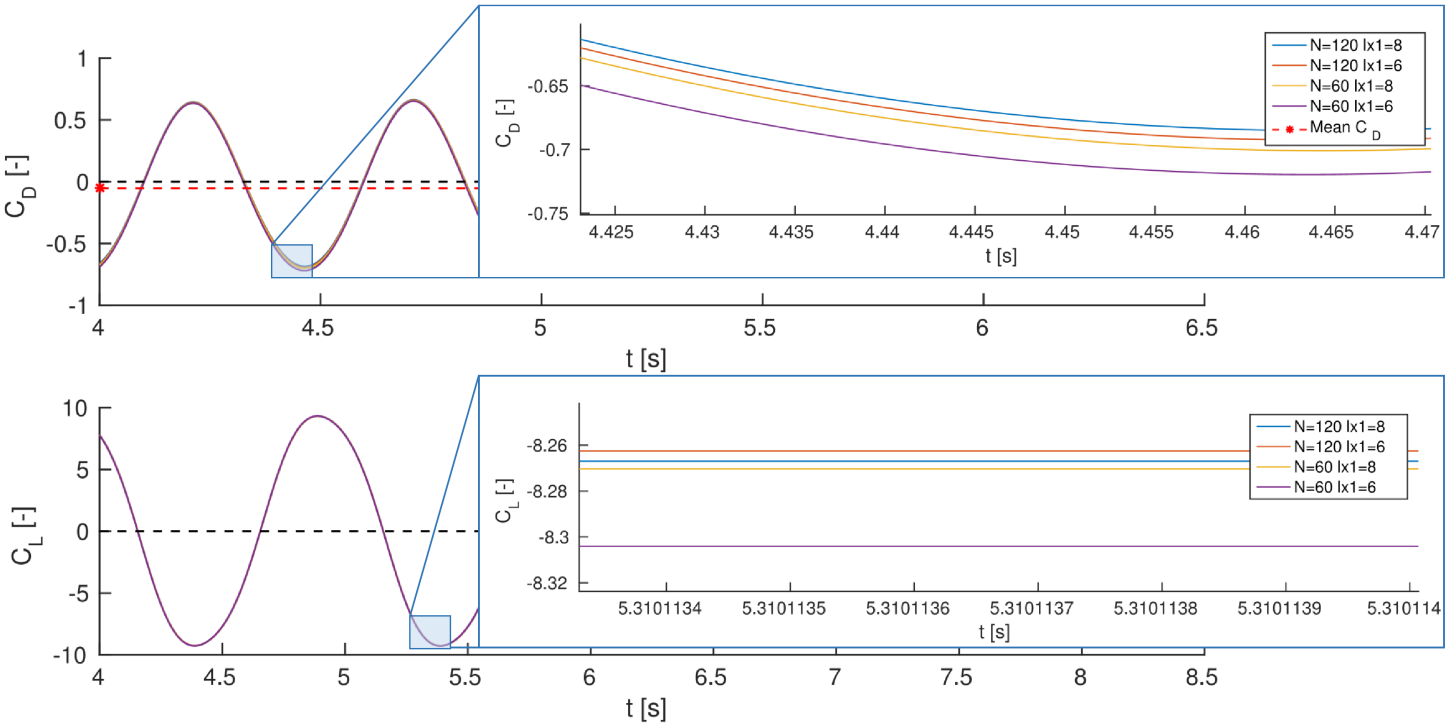

Figure 3.2: Aerodynamic coefficients convergence and zoom

	lx1=6	lx1=8
N=60	41.88	18.30
N=120	8.97	0

Table 3.1: Convergence Analysis: Drag Error (%)

	lx1=6	lx1=8
N=60	-89.82	-75.56
N=120	-48.7	0

Table 3.4: Convergence Analysis: Relative time difference (%)

	lx1=6	lx1=8
N=60	4.27	1.25
N=120	2.38	0

Table 3.2: Convergence Analysis: Lift Error (%)

	lx1=6	lx1=8
N=60	10.38	0.39
N=120	0.2	0

Table 3.5: Convergence Analysis: St_L Error ($\times 10^6$)

	lx1=6	lx1=8
N=60	0.8649	0.5231
N=120	0.4826	0

Table 3.3: Convergence Analysis: St_D Error ($\times 10^5$)

	lx1=6	lx1=8
N=60	42.10	18.35
N=120	9.27	0

Table 3.6: Convergence Analysis: Total Error (%)

We can conclude that refining the mesh gives more accurate results than using higher order polynomials. Unfortunately it also takes more time to compute the solution. It should be noted

that in this configuration the mean drag is negative, see Fig. 3.2, this means that the airfoil experiences thrust. A similar convergence analysis for the vvvO boundary conditions in given in appendix, see section A.1.

4 Symmetry breaking and initial condition reminiscence

Note that with this combined pitching and flapping motions the airfoil has a negative drag coefficient, $\bar{C}_D = -0.0527$, which means that the system experiences thrust. Moreover, with a harmonic and symmetric motion of a symmetric airfoil we observe a non-zero lift coefficient, namely $\bar{C}_L = 0.0210$. This is surprising since we assumed the flow to display a top down symmetry over the appropriate time period. Nevertheless, this assumption might not hold when the von Karman vortex street starts to align. For such an unexpected observation several questions must be answered.

Is the solution converged?

First, we must make sure that the solution is converged and that the unexpected result is not due to a lack of convergence. From Tab. 3.2 we can see that the lift coefficients differ only by a few percents when carrying out the convergence analysis. From this we can assume that the solution reached a converged state.

Does it depend on the domain size?

Secondly, in order to make sure that this lift generation does not depend significantly on the domain size (i.e. $D_1 : \{l_b = 12, h_b = 14\}$) and thus on the imposed boundary conditions, we try a simulation with a reduced domain $D_2 : \{l_b = 8, h_b = 9\}$. The results are shown in Tab. 4.1 in which both simulations are carried out with $N = 60$ and **lx1**=6.

	D1	**D2**
$\bar{\mathbf{C}}_\mathbf{D}$	-0.0748	-0.0767
$\bar{\mathbf{C}}_\mathbf{L}$	0.0201	0.0209

Table 4.1: Influence of a smaller domain on the aerodynamic coefficients

The relative errors are:

$$\eta_D = 2.5\% \qquad \eta_L = 3.9\% \tag{4.1}$$

Since they are rather small compared to the domain size reduction (approximately one third in both directions) we can consider that the lift is not due to an incoherent boundary condition. Indeed, a smaller domain size would enhance its effect.

Is this a symmetry breaking ?

Finally, to ensure that we deal with a symmetry breaking, we run the same simulation but starting with the mirror initial position:

$$\theta_0 = -0.16 \qquad A = -0.3 \tag{4.2}$$

The results are shown in Tab. 4.2 and Fig. 4.1.

	$(\mathbf{A}, \theta_\mathbf{0})$	$(-\mathbf{A}, -\theta_\mathbf{0})$
$\bar{\mathbf{C}}_\mathbf{D}$	-0.0748	-0.0748
$\bar{\mathbf{C}}_\mathbf{L}$	0.0201	-0.0202

Table 4.2: Aerodynamic coefficients for mirror initial position

On the first hand, we can see that the drag is not influenced by the different initial conditions, this means that it is not linked to the top-down symmetry. On the other hand, the lift displays the same magnitude but with an opposite direction. Hence, to reverse the initial condition reverses the force, see Fig. 4.1. This encourages the assumption of a lift force generated by a symmetry breaking which direction depends on the initial conditions.

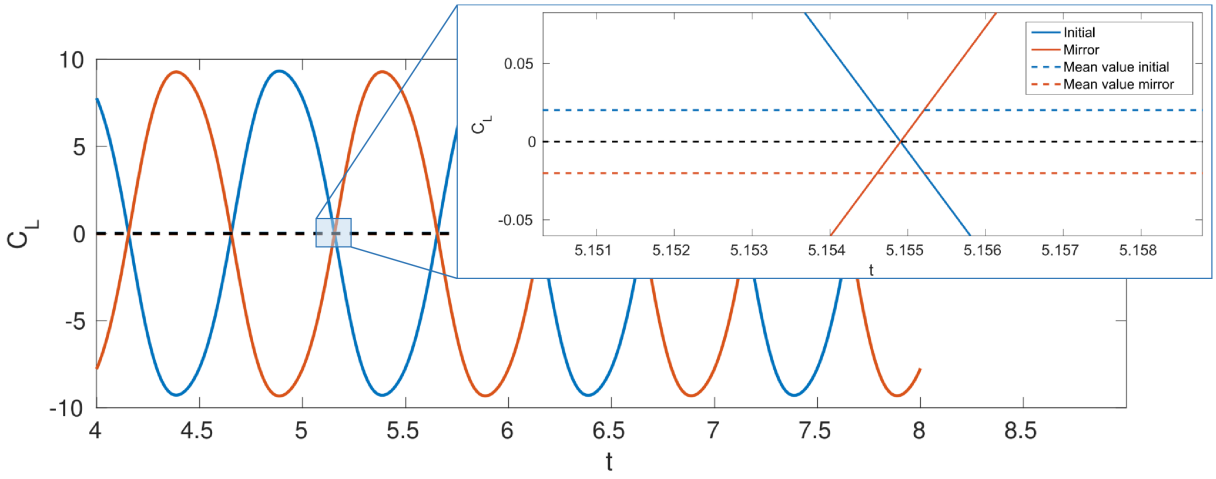

Figure 4.1: Comparison between two simulations with mirror initial conditions

It it important to notice that this phenomenon might not be present in real life and be only an artefact of our simulation. Indeed, it might be solely due to the inaccurate initial condition of the flow field defined in section 1.4.

5 An interesting combination of the motions

In this section we want to investigate the effect of combined pitching and flapping motions. At first, we will consider the two motions separately. Then, the combined motion is introduced and the effect of the phase-shift between pitching and flapping on thrust generation is explored. Specifically, we choose a set of parameters such that there is no thrust generation when only pitching or flapping are involved.

5.1 Two independent motions

The flapping motion: The parameters for the flapping motion are:

- $A = 0.3$
- $St_\omega = 1$
- $\alpha = 0$
- $Re = 100$
- BC=vvvv
- $N = 60$
- **lx1**=6

The results are shown in fig. 5.1 and tab. 5.1. The von Karman vortex street is slightly inverted but still the drag is positive. This is due to the friction drag that is not yet overcome by the pressure thrust. This has already been pointed out by Bastien Gorret in [1]. Also, a small lift is generated.

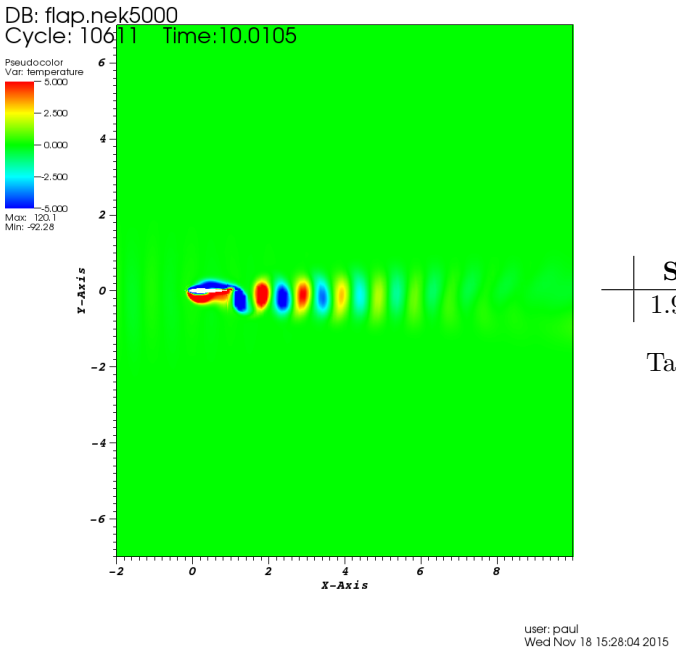

Figure 5.1: Flow configuration (absolute vorticity)

$\mathbf{St_D}$	$\mathbf{St_L}$	$\mathbf{\bar{C}_D}$	$\mathbf{\bar{C}_L}$
1.9936	1.0002	0.1614	0.0285

Table 5.1: Only flapping results

The pitching motion: The parameters for the pitching motion are:

- $\theta_0 = 0.16$
- $Re = 100$
- $N = 60$
- $St_\phi = 1$
- BC=vvvv
- **lx1**=6

The results are shown in fig. 5.2 and tab. 5.2. Here again, the von Karman vortex street is not aligned yet and the drag is greater. The lift on the other hand is smaller.

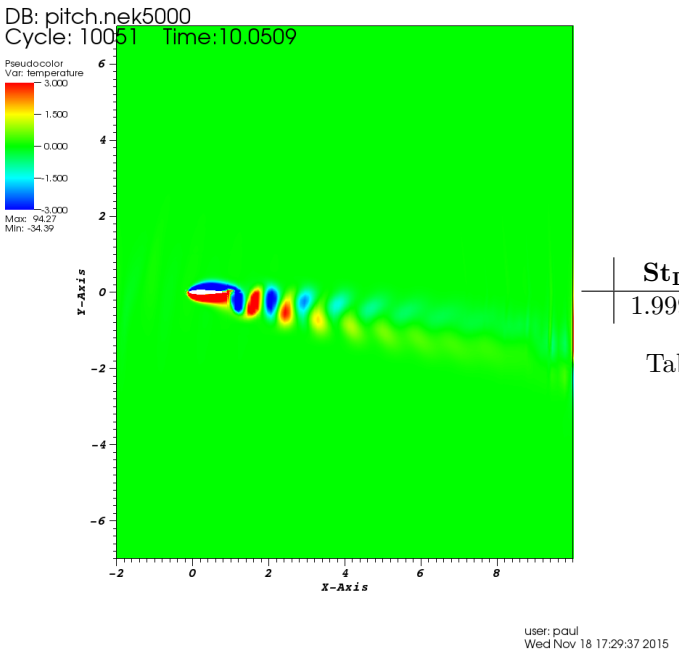

Figure 5.2: Flow configuration (absolute vorticity)

$\mathbf{St_D}$	$\mathbf{St_L}$	$\mathbf{\bar{C}_D}$	$\mathbf{\bar{C}_L}$
1.9999	1.0002	0.34788	0.011835

Table 5.2: Only pitching results

5.2 Combined motion

General parameters: The parameters for the combined motion are:

- $\theta_0 = 0.16$
- $St_\omega = St_\phi = St = 1$
- BC=vvvv
- $A = 0.3$
- $Re = 100$

Here we make a restriction of prime importance by setting the two oscillating frequencies to the same value.

Relevant values of the phase-shift: At this point we should take some time in order to determine the range of phase-shifts that we must study. Should we consider $\alpha \in [0, 2\pi]$ or can we restrict ourselves to $\alpha \in [0, \pi]$? To discuss this we plot cosinus functions for different phase-shifts in Fig. 5.3. Obviously, $\alpha = 0$ and $\alpha = 2\pi$ give an identical motion (the two blue curves are the same). Let's take this blue curve as the pitching motion which is independent of the phase-shift. Now we consider the relation between this motion and the pitching motions represented by the other curves. Fist, we focus on the red curves $\alpha = \frac{\pi}{4}$ and $\alpha = \frac{7\pi}{4}$. We can see that, even if the extreme positions of the two motion are separated by the same time duration, they do not share the same relation with the pitching motion. For $\alpha = \frac{\pi}{4}$ the flapping motion is "ahead" (in time) of the pitching motion : it already starts to go down while the foil is still pitching up (anti-clock wise rotation). On the contrary, for $\alpha = \frac{7\pi}{4}$, the flapping motion is "delayed" compared to the pitching one. The same discussion holds for the other phase-shifts. We will later see that this "delay" determines if the foil passes the $y = 0$ axis leading edge first or trailing edge first. We will also try to discuss how this difference might influence the behaviour of the drag coefficient.

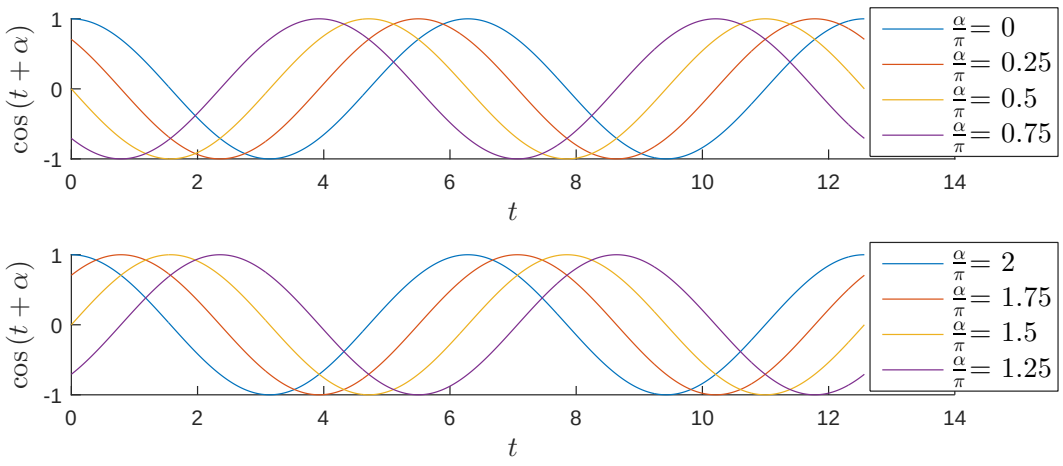

Figure 5.3: Shifted cosinus functions

Another important aspect is to know if the two motions are in phase or in opposite phase. For the cases $\alpha = 0$ or $\alpha = 2\pi$ the motions are perfectly in phase whereas they are totally in opposite phase for $\alpha = \pi$. It is more difficult to determine if the motions are rather in phase or rather out of phase for the other values of the phase-shift. One way to do it is to look at the sign of the product of the velocities. In other words we look at the sign of the function :

$$f(t) = \sin(t)\,\sin(t+\alpha) \tag{5.1}$$

If the function is positive during most of the period then the two motions are rather in phase. For example :

$$\alpha = 0, 2\pi \Rightarrow f(t) \geq 0 \quad \forall t \qquad \text{and} \qquad \alpha = \pi \Rightarrow f(t) \leq 0 \quad \forall t \tag{5.2}$$

From Fig. 5.4 we can see that the "delay" we mentioned earlier does not influence if the motion are in phase or not. Moreover the observation of this figure can be generalized : for $\alpha \in [-\frac{\pi}{2}, \frac{\pi}{2}] \bmod(2\pi)$ the two motions are rather in phase whereas they are more in opposite phase for $\alpha \in [\frac{\pi}{2}, \frac{3\pi}{2}] \bmod(2\pi)$.

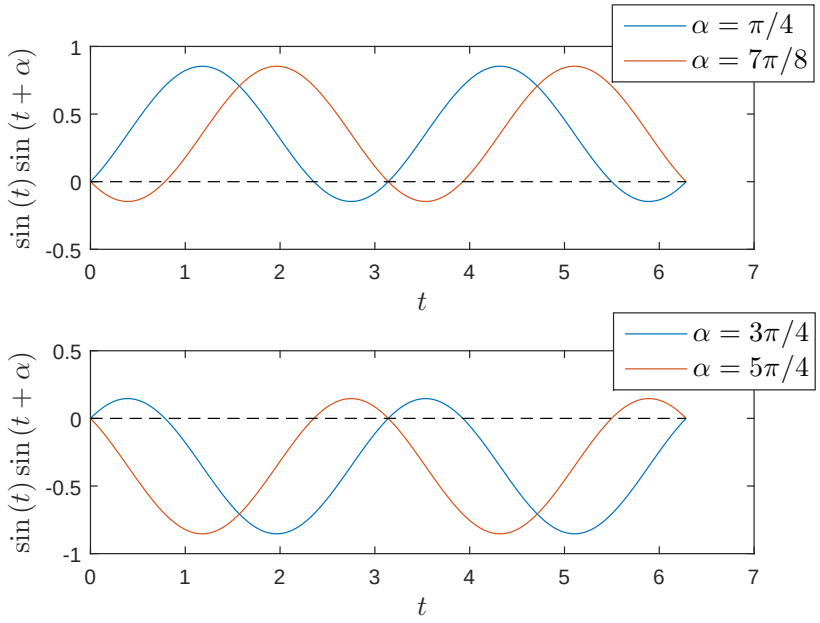

Figure 5.4: Velocity product between the pitching and shifted flapping motions

A more convenient way to observe what we just said is to have a look at the video `PhaseShifts.avi` given in the complementary files. On this video we can see the inclination at which the foil passes the horizontal axis and if the angular and translation velocities have same sign.

All this discussion highlights the fact that the motion is different over the whole $\alpha \in [0, 2\pi]$ range. This is due to the fact that the phase is only added to one of the two motions.

5.3 Phase-shift influence

We observed previously that the value of the lift coefficient was dependent on the initial condition, see section 4. This seemed not to be the case for the drag, however it is important to explicitly state how the different phase-shifts are introduced. We decide to carry out three simulations :

- `loop-forward`: One simulation of 135 seconds where we change the phase-shift α every 15 seconds. In this case α starts at 0 and increases up to 2π. This means that the initial condition defined in section 1.4 only applies to $\alpha = 0$. For the other phase-shifts the initial condition is the flow field associated with the previous phase-shift.
- `intermittent`: Here we make 8 separated simulation of 15 seconds. Therefore the initial condition of section 1.4 applies to all the phase-shifts.
- `loop-backward`: The same simulation as `loop-forward` but here α starts at 2π and decreases down to 0.

The results are shown in Fig. 5.5 and Tab. 5.3.

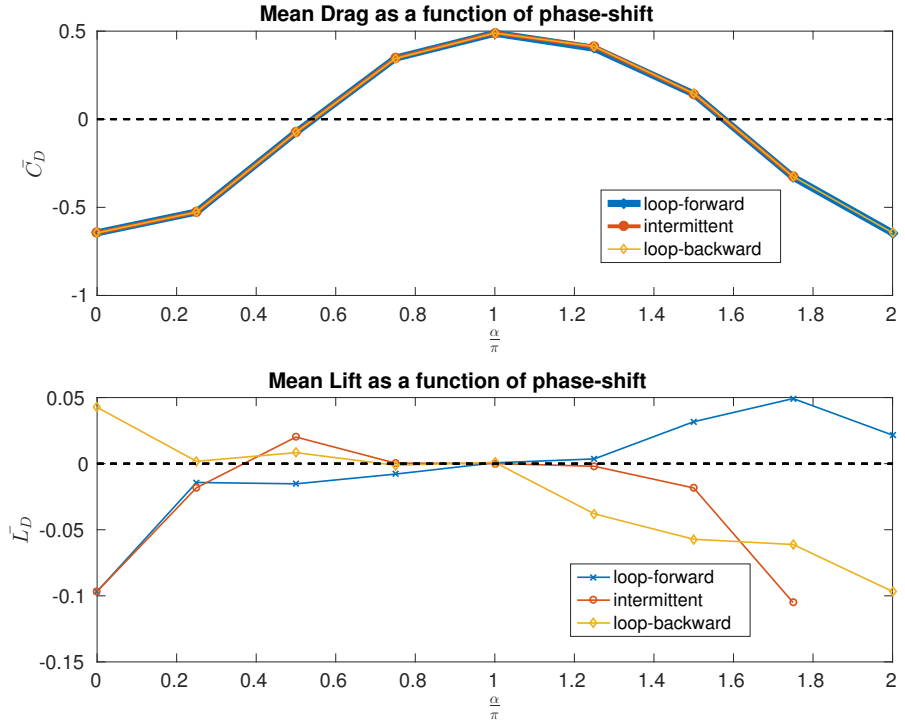

Figure 5.5: Phase-shift influence on combined motion

The first and major result is that we can produce thrust by combining two motions which, taken separately, generate drag. Moreover, depending on the phase-shift between these motions, we can either produce drag (positive drag coefficient) or thrust (negative drag coefficient).

From Fig. 5.5 we can see that the maximum thrust is obtained for $\alpha = 0$ and $\alpha = 2\pi$ and that the maximum drag is obtained for $\alpha = \pi$. Similarly, we obtain thrust for phase-shifts close to $\alpha = 0$ and drag for a phase-shifts close to $\alpha = \pi$. This can be understood from the discussion we made in subsec. 5.2. If the two motions are in phase, i.e. the two velocities have same sign over the most part of the motion, they "act" together in the generation of the vorticity. For example, when the foil is going up (positive flapping velocity) there is a production of negative vorticity at the trailing edge. Now, if at the same time the foil is pitching in the anti-clock wise direction (positive angular velocity), there is also generation of negative vorticity at the trailing edge and the two contributions add up. When this happens the production of vorticity is maximal and the reversion of the vortex street is greater. This yields more thrust. The two motions are perfectly in phase for $\alpha = 0$ and $\alpha = 2\pi$ for which the thrust is also the greater. On the contrary if the two motions are in opposite phase, they produce vorticity of opposite sign and therefore diminish the overall vorticity. This phenomenon is at its climax for $\alpha = \pi$.

Another interesting aspect is the fact that the drag curve is not symmetric around π. This confirms the importance of the "delay" between the two motions that we highlighted in subsec. 5.2. It is observed that the configurations with $\alpha \in [0, \pi]$ tend to produce more thrust than the ones with $\alpha \in [\pi, 2\pi]$. In the first case we have that the flapping motion is in advance compared to the pitching one and thus the foil crosses the horizontal axis with the configuration shown in Fig. 5.6. U is the free-stream velocity and v_{rel} is the velocity due to the flapping motion only. The sum of these velocities, v_{tot} makes an angle ψ with the foil chord-wise direction. For such a configuration there is a lift $\mathbf{L}$ and a drag $\mathbf{D}$ generated. We can see that the projection of $\mathbf{L}$ in the $\mathbf{x}$ axis is negative and is therefore interpreted as thrust.

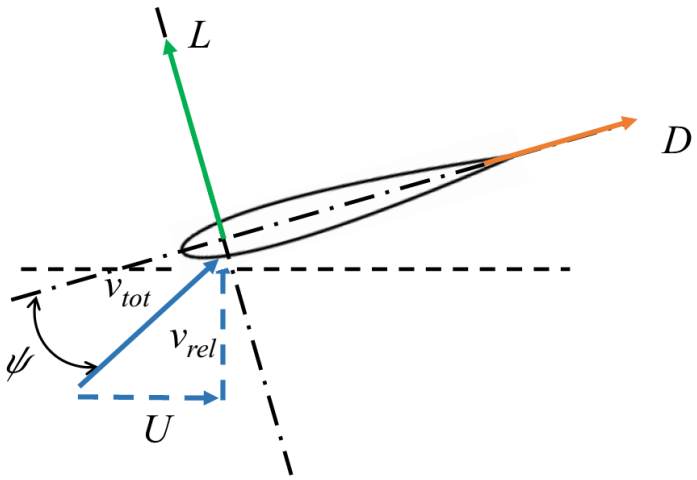

Figure 5.6: Configuration for a foil going down for $\alpha \in [0, \pi]$

On the other hand, if we have $\alpha \in [\pi, 2\pi]$ we get the configuration displayed in Fig. 5.7. And in this case the projection on the **x** axis of **L** is positive and adds to the drag. This could explain the lack of symmetry around π of the drag coefficient in Fig. 5.5 and why configurations with $\alpha \in [0, \pi]$ produce more thrust.

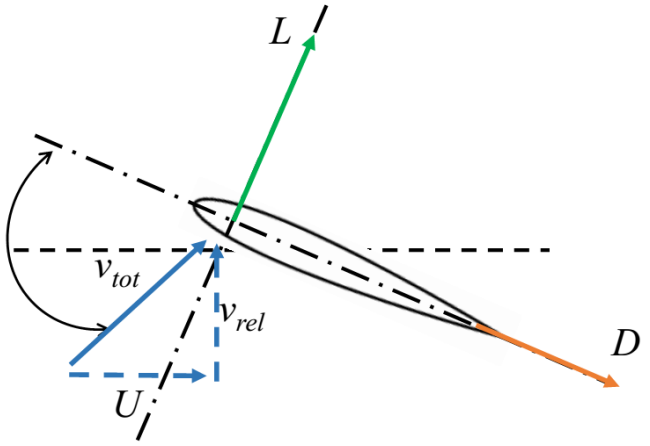

Figure 5.7: Configuration for a foil going down for $\alpha \in [\pi, 2\pi]$

From Fig. 5.5 we get that all the curves superimpose and hence the drag is not greatly influenced by the initial conditions. However, note that on the `loop-forward` (and `loop-backward`) the aerodynamic forces for $\alpha = 0$ and $\alpha = 2\pi$ are different because of different initial conditions, see Tab. 5.3. In order to make sure that this deviation is indeed due to the influence of different initial conditions we simulate separately $\alpha = 0$ and $\alpha = 2\pi$. Thus, making sure that the initial condition is the same. We find then that the difference is of order 10^{-12}.

$\boldsymbol{\alpha}$ [rad]	$\mathbf{St_D}$	$\mathbf{St_L}$	$\bar{\mathbf{C}}_\mathbf{D}$	$\bar{\mathbf{C}}_\mathbf{L}$
0	2.0030	1.0001	-0.6455	-0.0972
$\pi/4$	2.0004	1.0000	-0.5267	-0.0127
$\pi/2$	1.9998	0.9999	-0.0746	-0.0141
$3\pi/4$	1.9999	0.9999	0.3465	-0.0060
π	2.0003	1.0000	0.4879	0.0004
$5\pi/4$	1.9991	0.9999	0.4038	0.0040
$3\pi/2$	1.9993	1.0000	0.1443	0.0294
$7\pi/4$	1.9984	1.0001	-0.3272	0.0411
2π	1.9989	1.0000	-0.6447	0.0168

Table 5.3: Results for `loop-forward` simulation

It is hard to identify a clear pattern for the lift coefficient in Fig. 5.5. We can claim however that is is highly dependent on the initial conditions. Moreover the `loop-forward` and `loop-backward` result in opposite signs but also different magnitudes. The `intermittent` does predict a negative lift most of the time. The lift generation seems to be greater around $\alpha = 0$ and $\alpha = 2\pi$ when the thrust is at its peak and the von Karman vortex street is the most inverted. Rather, the lift is almost null around $\alpha = 0$ when the von Karman vortex street is not inverted.

6 Conclusion

In this work we have considered the combined pitching and flapping motion of a NACA0012 subjected to an incoming flow. The vortex dynamics observed in our simulations are in agreement with the results of [5], where a flapping ellipse was studied. Specifically the thrust generation is associated with a reversed Von-Karman wake which modifies the mean axial velocity to a jet profile (see [5]).

We have considered an interesting case of combined pitching/flapping motion where no thrust is generated when either the pitching or the flapping is turned off. Interestingly when pitching and flapping are superimposed, the thrust generation strongly depends on the phase shift between the two, α. In particular at $Re = 100$ thrust is generated if α is approximately in the range $\alpha \in [-\pi/2, \pi/2]$. In contrast, a mean drag is obtained for $\alpha \in [\pi/2, 3\pi/2]$. Specifically, the optimal phase for thrust generation results $\alpha_{opt} = 0$ which is associated to a thrust coefficient equal to 0.6. Moreover it has been observed that eventhought the airfoil and the motion are symmetric, the lift coefficient is not null. This is due to a symmetry breaking [5] occurring in the vortex shedding behind the airfoil which depends on the initial condition.

However, the optimal phase for thrust generation α is supposed to depend on the flow regime and the Reynolds number, as shown in the literature ([6], [7] and [8]). Specifically, [7] finds that the higher thrust coefficient is for a phase shift of 90°. Similarly, [8] find a maximum thrust for 90° at low flapping frequencies and at 180° for high frequencies. Yet, they also derived that the optimum propulsive efficiency was archived for a phase-shift of 0° as the frequency and pitching/flapping amplitude increased. They therefore show that there is also a dependency on the frequency. These results are quite different from what we found here but might be explained by a different Reynolds and/or frequency. Furthermore, the ratio between the amplitudes of the two motions might influence the optimal phase-shift. This gives some interesting leads to follow in the future: monitor the propulsive efficiency and investigate the Reynolds and frequency dependency as well as the effect of the amplitude ratio. The impact of different frequencies between the two motions should also be challenging and can be exploited with the numerical tools we have developed.

Appendix

A Validation of the numerical tools

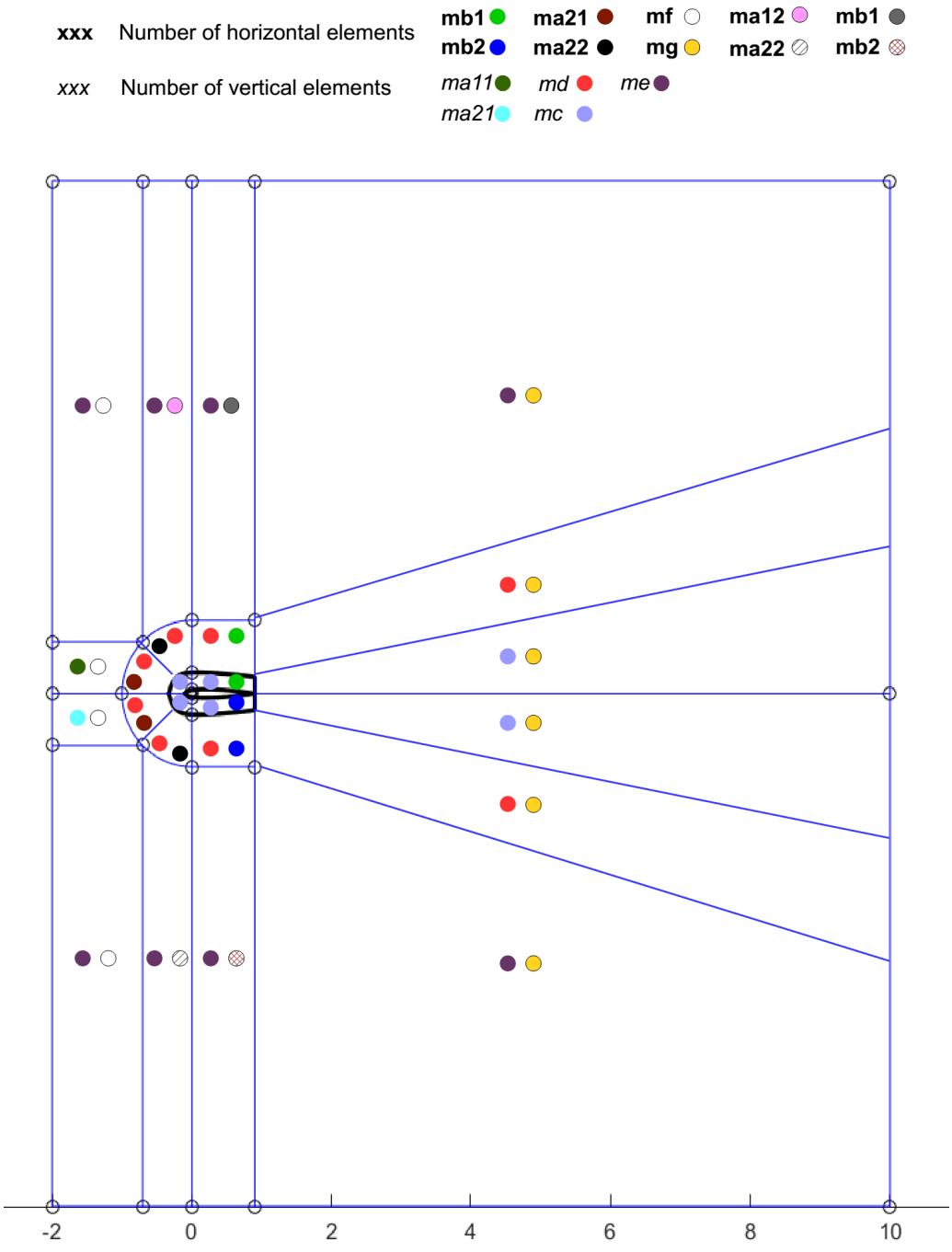

Figure A.1: Distribution of the mesh cells along the simulation domain

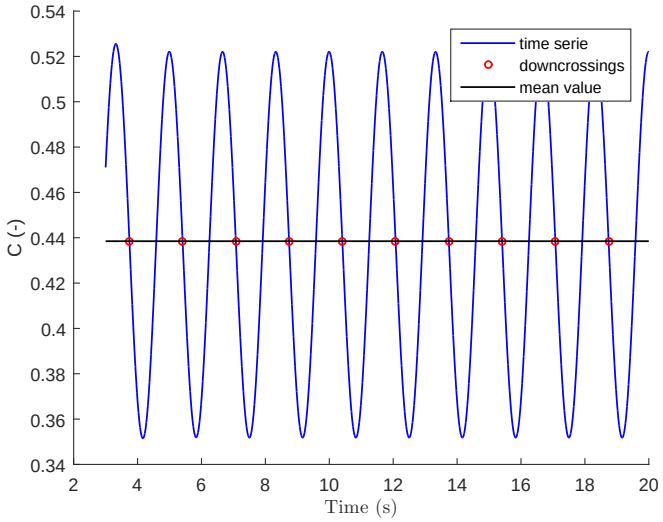

Figure A.2: Analysis on at regime solution for Drag

A.1 vvvO boundary condition

Here, the convergence analysis is carried out with the following parameters :

- $\theta_0 = 0.12$
- $St_\omega = St_\phi = St = 0.3$
- $Re = 100$
- $A = 0.4$
- $\alpha = \pi$

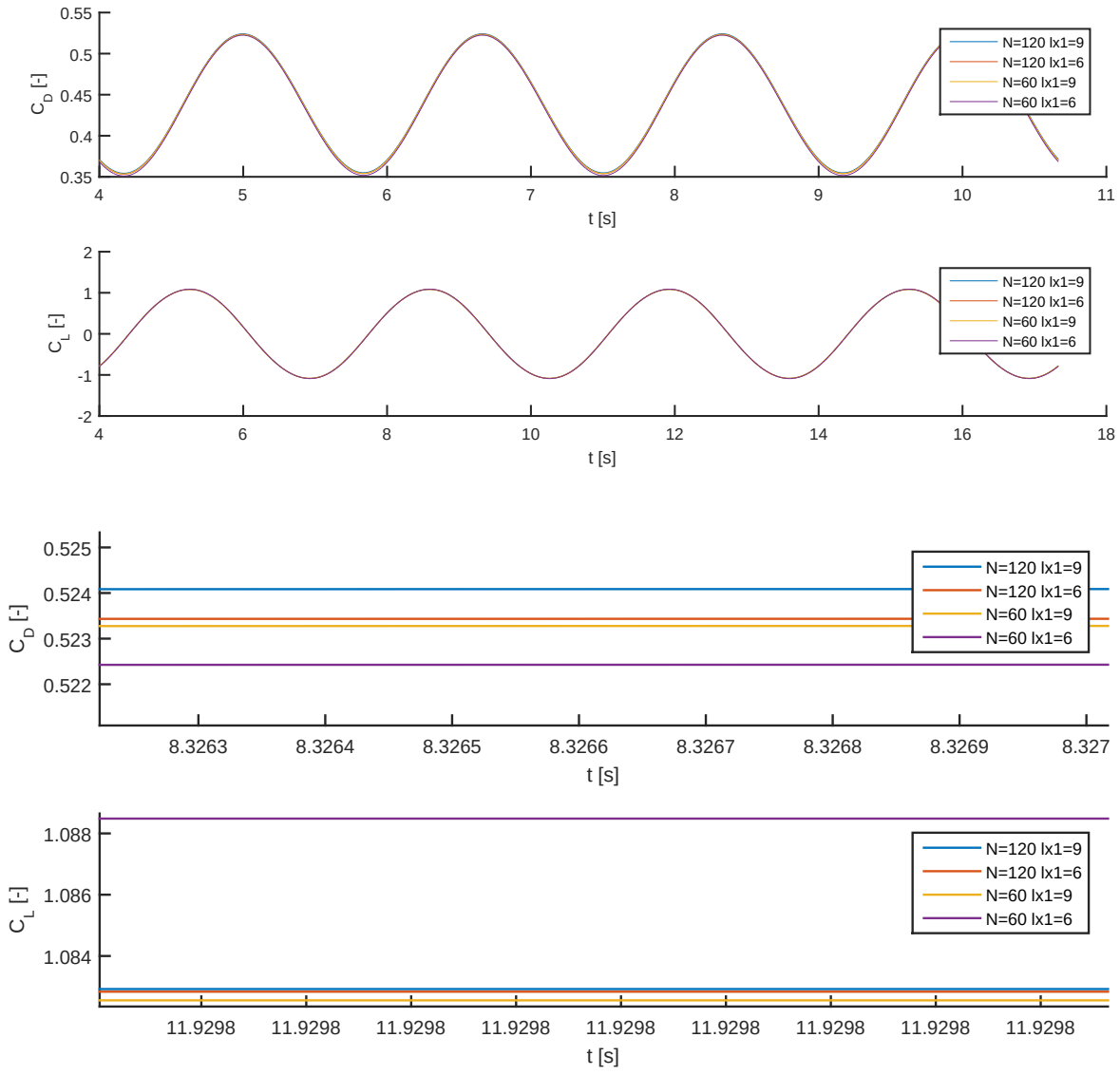

Figure A.3: Aerodynamic coefficients convergence and zoom

	lx1=6	**lx1=9**
N=60	0.56	0.18
N=120	0.19	0

Table A.1: Convergence Analysis: Drag Error (%)

	lx1=6	**lx1=9**
N=60	2.87	0.28
N=120	3.28	0

Table A.2: Convergence Analysis: Lift Error (%)

	lx1=6	**lx1=9**
N=60	0.1766	0.1252
N=120	0.1425	0

Table A.3: Convergence Analysis: St_D Error ($\times 10^5$)

	lx1=6	**lx1=9**
N=60	0.6009	0.0734
N=120	0.0146	0

Table A.4: Convergence Analysis: St_L Error ($\times 10^6$)

	lx1=6	**lx1=9**
N=60	-89.33	-32.11
N=120	-26.81	0

Table A.5: Convergence Analysis: Relative time difference (%)

	lx1=6	**lx1=9**
N=60	2.92	0.33
N=120	3.28	0

Table A.6: Convergence Analysis: Total Error (%)

As we can see from fig. A.3 the solution at regime converges toward the most accurate one. The two solutions ($N = 60$, $\mathbf{lx1} = 9$) and ($N = 120$, $\mathbf{lx1} = 6$) are rather close with a slight advantage for the finer mesh. If we have a look at the error they are almost equivalent for the prediction of the drag (the value of interest). However, the solution ($N = 120$, $\mathbf{lx1} = 6$) exhibits a large error in its prediction of the lift coefficient which yields a large total error. There might be several causes for this, a inaccurate mesh, a problem in our calculation of the lift coefficient from the results or simply a "oscillating" convergence. Moreover, since the lift coefficient is small, i.e. should be around zero from symmetry, a small deviation can trigger a large relative error. This is not of main importance as the study focuses on the drag coefficient. In order to get a better overview of the convergence properties of the system it would be necessary to carry out more simulations. The finer mesh is a bit faster than the higher order polynomials. We may conclude that the two parameters tuning are equivalent with a preference for the finer mesh if we are only interested in the drag coefficient. With this choice of parameters the flow pattern is shown in fig. 2.5 and is a Karman vortex street. From the drag coefficient displayed in tab. 2.1 we can see that this flow configuration does not generate thrust, therefore it is not of main importance for the present study. Unfortunately, the configurations generating thrust (i.e. reversed vortex street) shown in fig. 3.1 requires higher Strouhal number and pitching amplitudes. For such higher values the vvvO boundary condition is not convergent any more : the high frequency and amplitude of the oscillating motion generates a tangential velocity proportional to the distance from the center of rotation. Thus high velocities are obtained at the limit of the computational domain and in its corners. This affects the sensitive O boundary condition. It should be noted that here the errors are smaller than in the vvvv convergence analysis. This may be due to a more complex flow configuration or to the fact that the vvvv boundary condition holds less physical meaning. In both cases the solution would require more computational effort to satisfyingly converge.

B Complementary files

- `PhaseShifts.avi`

References

[1] Bastien Gorret. The generation of thrust and lift through the flapping motion of naca profiles. *Semester Project EPFL*, 2015.

[2] Robin Luthi. Study of the flow around a 2d pitching foil. *Semester Project EPFL*, 2015.

[3] Mathematics and Computer Science Division. *Nek5000 User Documentation*. Technical report, **Argonne National Laboratory**. URL `http://nek5000.github.io/NekDoc/Nek_users.pdf`.

[4] Software. URL `http://www.ansys.com/Products`.

[5] Tomasz Kozlowski and Henryk Kudela. Transitions in the wake behind the plunging profile. *Fluid Dynamic Research*, 2014.

[6] Chang kwon Kang, Yeon Sik Baik, Luis P. Bernal, Wei Shyy, and Michael V. Ol. Fluid dynamics of pitching and plunging airfoils of reynolds number between 1×10^4 and 6×10^4. *47th AIAA*, January 2009.

[7] Dr. Alex Povitsky. Modeling of aerodynamics of flapping wings and blades using high-order of approximation numerical schemes and lattice boltzmann method. *AMS Seminar Series, NASA Ames Research Center*, October 5, 2015.

[8] Strouhal number characerisation of combined pitching and plunging motion. URL `http://louisville.edu/speed/cfdlab/files/08chapter7.pdf/at_download/file`.